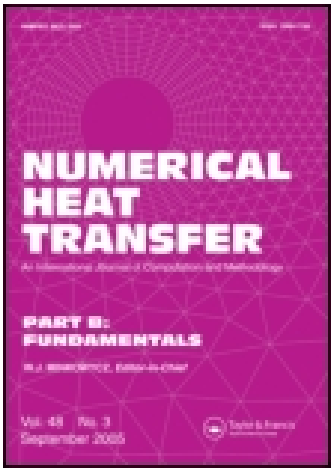

Numerical Heat Transfer, Part B: Fundamentals: An International Journal of Computation and Methodology
Publication details, including instructions for authors and subscription information:
http://www.tandfonline.com/loi/unhb20

A Finite-Volume-Based Approach for Dynamic Fluid-Structure Interaction

Yeng-Yung Tsui [a], Yi-Cheng Huang [a], Chun-Lung Huang [a] & Shi-Wen Lin [a]
[a] Department of Mechanical Engineering, National Chiao Tung University, Hsinchu, Taiwan, Republic of China
Published online: 08 Oct 2013.

To cite this article: Yeng-Yung Tsui, Yi-Cheng Huang, Chun-Lung Huang & Shi-Wen Lin (2013) A Finite-Volume-Based Approach for Dynamic Fluid-Structure Interaction, Numerical Heat Transfer, Part B: Fundamentals: An International Journal of Computation and Methodology, 64:4, 326-349, DOI: 10.1080/10407790.2013.806691

To link to this article: http://dx.doi.org/10.1080/10407790.2013.806691

Numerical Heat Transfer, Part B, 64: 326–349, 2013

ISSN: 1040-7790 print/1521-0626 online
DOI: 10.1080/10407790.2013.806691

Taylor & Francis
Taylor & Francis Group

A FINITE-VOLUME-BASED APPROACH FOR DYNAMIC FLUID-STRUCTURE INTERACTION

Yeng-Yung Tsui, Yi-Cheng Huang, Chun-Lung Huang, and Shi-Wen Lin

Department of Mechanical Engineering, National Chiao Tung University, Hsinchu, Taiwan, Republic of China

It is common to adopt finite-element methods to solve solid mechanics problems and finite-volume methods for fluid dynamics computations. The use of different methods causes complication of the solution procedure for problems involving both fluids and solids. In this study, a partitioned approach based on the finite-volume method for dynamic fluid–structure interaction is presented. The method is formulated in a way suitable for an unstructured mesh with arbitrary grid geometry. The variables for the fluid are stored at the centroids of grid cells, whereas those for the solid at the grid nodes. The latter arrangement makes it more suitable for large structure deformation. After spatial discretization for the solid using the finite-volume approach, the resulting system of ordinary differential equations is solved implicitly using the dual-time-stepping scheme. As for the fluid calculation, a pressure-based algorithm is employed and the time step is advanced in a prediction-correction manner. The finite-volume method for the solid is assessed by calculating the deformation and dynamics of a cantilever under various loads. Good agreement with analytical solutions is obtained. Then, the solution procedure is applied to two cases with coupled fluid flow and structure dynamics. One is the flow over a vertical plate with one end fixed on the floor in a channel. The other is the flow over a cylinder with a plate attached to it on the lee side.

1. INTRODUCTION

Finite-element methods have become the method of choice in analysis of structural mechanics because most problems in this field are self-adjoint. Finite-element methods feature the use of polynomial functions as shape functions to describe the variation of variables in contiguous elements and for the weighting procedure. However, the resulting stresses lose continuity across the inter-element boundaries due to the piecewise continuity of the shape functions. Another drawback of the method is that the conservation principle is satisfied only in a global sense, not in each cell. Usually, finite-element methods are regarded as being more accurate than finite-difference or finite-volume methods because high-order polynomials can be

Received 6 March 2013; accepted 23 April 2013.
The long-term financial support of the National Science Council, Republic of China, is acknowledged.
Address correspondence to Yeng-Yung Tsui, Department of Mechanical Engineering, National Chiao Tung University, 1001 Tu-Hsinch Road, Hsinchu 300, Taiwan, Republic of China. E-mail: yytsui@mail.nctu.edu.tw

NOMENCLATURE

$\vec{b}$	body force
c	damping coefficient
$\vec{d}$	displacement vector
E	Young's modulus
I	second moment of area
$\dot{m}$	mass flux
$\vec{n}$	unit normal vector
p	pressure
S	source term
t	time
$\vec{t}_B$	traction force
$\vec{v}$	solid velocity
$\vec{V}$	fluid velocity
$\vec{V}_g$	grid velocity
w_o	load constant
γ	blending factor
$\vec{\delta}_{cb}$	distance vector from c to b
$\Delta\vec{S}$	surface vector
$\Delta\forall$	cell volume
$\Delta\forall_f$	volume swept by the moving grid
ε	strain
ς	damping ratio
μ	viscosity
υ	Poisson's ratio
ρ	density
σ	stress
τ	pseudo time
ϕ	an entity
ω	natural circular frequency

Subscripts

b	boundary face
c	neighboring cell
f	cell face
P	primary cell

Superscripts

l	iteration index
m	pseudo-time step
n	new time step
o	old time step
$'$	first correction
$''$	second correction
$*$	prediction value
$**$	first correction value
$***$	second correction value

employed. However, in the Galerkin formulation it is often necessary to utilize linear shape function, and finite-element methods become equivalent to finite-volume methods in many cases [1, 2].

Fluid flows are usually convection-dominant and, thus, non-self-adjoint. This problem can easily be tackled in finite-volume methods. Similar to finite-element methods, unstructured grids are allowed to be used by finite-volume methods and, therefore, complex geometries can also easily be handled. Compared to the finite-element methods, their formulations are relatively simple and the conservation principle is strictly obeyed during discretization. In addition, finite-volume methods become very efficient in terms of computer memory and computing time because the generated matrices are sparse and effective, so iterative relaxation algorithms can be adopted. Therefore, they enjoy great popularity in computational fluid dynamics.

In recent years, developments in finite-volume methods have also been made to solve problems in solid mechanics. In some such works, the primitive variables, i.e., the displacements of structure, are placed on the centroids of the cells formed by grid lines and these cells are used for finite-volume discretization [3–7]. This cell-centered arrangement is widely applied in the context of fluid flow computations. However, since the geometry of the solid is described by the grid nodes on the boundaries, it suffers from difficulties in dealing with large deformation. It was assumed that the displacements are small and the computational grids are fixed without change in the analyses of the above-referred studies. In order to cope with the possibility of large deformation of the structure, it is better to store the variables at cell vertices, i.e., the grid nodes. The control volumes for the cell vertices are constructed from

the median dual grid. The approach developed by the group of Baily and Cross [8–10] is regarded as a finite-element–based finite volume method in which linear shape functions are employed for spatial discretization. In the alternative adopted by Xia and his colleagues [11–13], the stresses applied on the control surfaces are estimated using finite-difference approximations.

In a wide range of engineering systems, it is needed to consider the coupling of fluid flow and structural mechanics. Research efforts in this area have intensified recently. Demirdzic and Muzaferija [14] presented a cell-centered finite-volume method to analyze the coupled fluid flow, heat transfer, and stress in an air-cooled, two-stroke internal combustion engine. In the study by Greenshields and Weller [15], the cell-centered finite-volume method was applied to examine the wave propagation in a flexible tube and its effects on the fluid flow in the tube. Stein et al. [16] developed a computational strategy for a 3-D simulation of parachute fluid–structure interaction using the finite-element method. The finite-element method was adopted by Afrasiab et al. [17] to analyze the performance of a pneumatically actuated diaphragm microvalve and also by De Hart et al. [18] to investigate the interaction of blood flow with the operation of the aortic valve. In the study of Gluck et al. [19], a textile tent roof under the condition of high wind speed was examined. Three codes were employed in their simulation: a finite-volume code for fluid flow, a finite-element code for the solid structure, and a code for data exchange between the two computational codes. In the implicit partitioned approach by Sternel et al. [20], the solution tasks in the partitioned domains are carried out using different codes as well.

It is clear that with the use of different numerical approaches to deal with fluid dynamics and structure mechanics in multi-physics problems, the computational procedure becomes complicated. Transferring and filtering of data between different meshes and solution procedures may cause difficulties to achieve solution convergence. It is demanded to have a consistent solution method in both the fluid and solid domains. To pursue this goal, a finite-volume–based solution procedure is developed in this study. The mesh used for discretization is arranged in the cell-centered manner for fluid flows while the cell-vertex arrangement is employed for solid structures. In this way, both the meshes for the fluid and solid can easily be adapted to follow the deformation of the structure. Unlike other cell-vertex finite-volume methods, the formulation of the method in this work can be applied to grids of arbitrary topology, not restricted to quadrilateral or triangular grids. In addition, it is equally applicable to three-dimensional problems without any need for modification.

2. MATHEMATICAL MODELS

2.1. Formulations for Structural Dynamics

The equation governing the dynamics of a solid structure is given by Cauchy's equation,

$$\rho \frac{\partial^2 \vec{d}}{\partial t^2} = \nabla \cdot \sigma_{ij} + \vec{b} \tag{1}$$

where σ_{ij} is the stress tensor, $\vec{d}$ is the displacement vector, ρ is the density, and $\vec{b}$ is the body force. For the structures considered in this study the body forces are negligible. In some structure dynamics problems, the damping effects need to be considered. Damping is the ability of a structure system to dissipate energy. For a linear damper, the damping is proportional to the structure velocity. Then, the equation can be cast into the form

$$\frac{\partial \vec{v}}{\partial t} = \frac{1}{\rho} \nabla \cdot \sigma_{ij} - \frac{c\vec{v}}{\rho} \tag{2}$$

where $\vec{v}$ is the velocity of the structure and c is the coefficient of damping.

The relationship between stress and strain is the generalized Hooke's law, which, for an isotropic homogeneous material, can be expressed as

$$\begin{pmatrix} \sigma_{xx} \\ \sigma_{yy} \\ \sigma_{xy} \end{pmatrix} = \frac{E(1-\upsilon)}{(1+\upsilon)(1-2\upsilon)} \begin{bmatrix} 1 & \frac{\upsilon}{1-\upsilon} & 0 \\ \frac{\upsilon}{1-\upsilon} & 1 & 0 \\ 0 & 0 & \frac{1-2\upsilon}{2(1-\upsilon)} \end{bmatrix} \begin{pmatrix} \varepsilon_{xx} \\ \varepsilon_{yy} \\ \varepsilon_{xy} \end{pmatrix} \tag{3}$$

where E is Young's modulus and υ is Poisson's ratio. To allow large deformation, the strain is related to the displacement gradient via the Green-Lagrange relationship,

$$\begin{pmatrix} \varepsilon_{xx} \\ \varepsilon_{yy} \\ \varepsilon_{xy} \end{pmatrix} = \frac{1}{2} \begin{pmatrix} 2\frac{\partial d_x}{\partial x} + \left(\frac{\partial d_x}{\partial x}\right)^2 + \left(\frac{\partial d_y}{\partial x}\right)^2 \\ 2\frac{\partial d_y}{\partial y} + \left(\frac{\partial d_x}{\partial y}\right)^2 + \left(\frac{\partial d_y}{\partial y}\right)^2 \\ \frac{\partial d_x}{\partial y} + \frac{\partial d_y}{\partial x} + \frac{\partial d_x}{\partial x}\frac{\partial d_x}{\partial y} + \frac{\partial d_y}{\partial x}\frac{\partial d_y}{\partial y} \end{pmatrix} \tag{4}$$

where d_x and d_y are the displacements in the two directions of the Cartesian coordinate system.

The structure is subject to two kinds of boundary conditions on the surface of the solid domain: prescribed displacements $\vec{d}_B$ and prescribed tractions $\vec{t}_B$.

$$\vec{d} = \vec{d}_B \tag{5a}$$

$$N_{ij}\sigma_j = \vec{t}_B \tag{5b}$$

Here $\sigma_j = [\sigma_{xx}, \sigma_{yy}, \sigma_{xy}]^T$ is the stress vector and N_{ij} is the matrix of normal vectors,

$$N_{ij} = \begin{pmatrix} n_x & 0 & n_y \\ 0 & n_y & n_x \end{pmatrix} \tag{6}$$

where n_x and n_y are the components of the unit outward vector normal to the boundary.

2.2. Formulations for Fluid Dynamics

In order to cope with the continuous deformation of the structure, the computational grid for the fluid flow is allowed to move accordingly. The conservation equations for continuity and momentum in integral form [21] can be written as

$$\frac{\partial}{\partial t}\int_{\forall} \rho \, d\forall + \int_S \rho\left(\vec{V} - \vec{V}_g\right) \cdot d\vec{S} = 0 \tag{7}$$

$$\frac{\partial}{\partial t}\int_{\forall} \rho \vec{V} \, d\forall + \int_S \rho \vec{V} \otimes \left(\vec{V} - \vec{V}_g\right) \cdot d\vec{S} = \int_S (\mu \nabla \vec{V}) \cdot d\vec{S} - \int_{\forall} \nabla p \, d\forall \tag{8}$$

where ρ is the fluid density, p is the pressure, μ is the viscosity, $\vec{v}$ is the fluid velocity, and $\vec{v}_g$ is the grid velocity. The grid, which moves in space, must also obey the conservation law [22]:

$$\frac{\partial}{\partial t}\int_{\forall} d\forall - \int_S \vec{V}_g \cdot d\vec{S} = 0 \tag{9}$$

Multiplying the space conservation equation by ρ and subtracting it from Eq. (7) leads to

$$\int_S \rho \vec{V} \cdot d\vec{S} = 0 \tag{10}$$

which means that there is no need to consider the grid velocity in the continuity equation.

The cases tested for fluid–structure interaction include an elastic beam being placed in a channel. No-slip condition is imposed on solid walls. Flow rate is specified at the inlet of the channel and convective boundary condition is assigned at the outlet:

$$\frac{\partial \phi}{\partial t} + V_c \frac{\partial \phi}{\partial x} = 0 \tag{11}$$

where ϕ represents a flow entity and V_c the convective velocity.

3. NUMERICAL METHODS FOR STRUCTURE

3.1. Discretization

The control volume at a grid node P in the computational mesh for the solid is shown in Figure 1*a*. It is constructed by connecting the centroids of the cells which share this node as a common vertex. With use of the Gauss divergence theorem and the mean-value theorem, the integration of Eq. (2) over the control volume can be approximated by

$$\frac{\partial u}{\partial t} = \frac{1}{\rho \, \Delta\forall} \sum_f \left[\lambda(1-\upsilon)\varepsilon_{xx} + \lambda\upsilon\varepsilon_{yy}\right]_f \Delta S_x + \left[\mu\varepsilon_{xy}\right]_f \Delta S_y - \frac{cu}{\rho} \tag{12a}$$

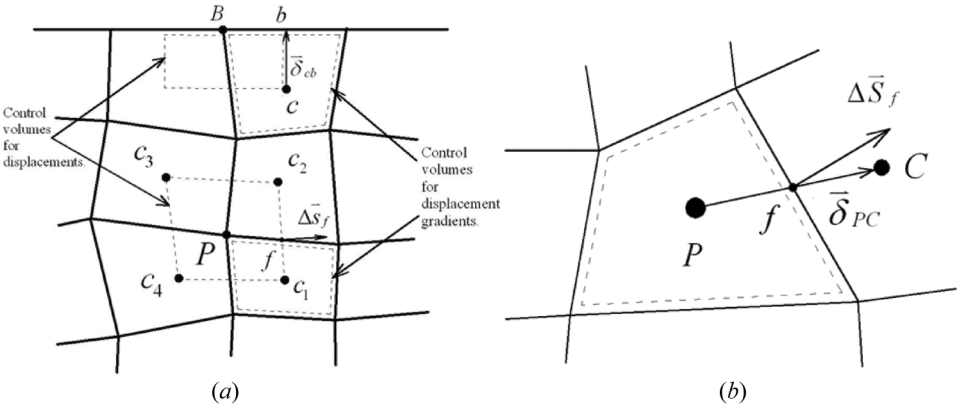

Figure 1. Control volumes for (*a*) structure and (*b*) fluid calculations.

$$\frac{\partial v}{\partial t} = \frac{1}{\rho\,\Delta\forall}\sum_f \left[\lambda\upsilon\varepsilon_{xx} + \lambda(1-\upsilon)\varepsilon_{yy}\right]_f \Delta S_y + \left[\mu\varepsilon_{xy}\right]_f \Delta S_x - \frac{cv}{\rho} \tag{12b}$$

where the coefficients $\lambda = E/(1+\upsilon)(1-2\upsilon)$ and $\mu = E/2(1+\upsilon)$, the subscript f denotes the face of the control volume, ΔS_x and ΔS_y are the components of the surface vector, and $\Delta\forall$ is the volume of the control volume. The sum is taken over all the faces of the control volume.

To complete discretization, the gradients of displacements need to be estimated. Different from the displacements, the gradients are stored at the centroid of each grid cell (see Figure 1*a*). Applying the divergence theorem to the cell volume leads to

$$\nabla\phi = \frac{1}{\Delta\forall}\sum_f \phi_f \Delta\vec{S}_f \tag{13}$$

where ϕ represents displacement component and $\Delta\vec{S}_f$ is the surface vector of face f. The face value ϕ_f is obtained from the mean of the nodal values which are stored on the vertices of the face (or the two end nodes of the edge in 2D). The gradients on the face required in Eq. (12) are then approximated by the mean of the gradients at the cell centroids used to construct this face.

Care must be taken for the nodes on boundaries. As shown in Figure 1*a*, the control volume for a boundary node B occupies half the width of the mesh. Traction forces are exerted over the boundary surface. The displacement gradients at the boundary face centroid b are required for integration over the face cb. The gradients at b are estimated via the relation

$$\nabla\phi_b = \nabla\phi_c + \nabla(\nabla\phi)\cdot\vec{\delta}_{cb} \tag{14}$$

where $\vec{\delta}_{cb}$ denotes the distance vector from c to b. The gradients of $\nabla\phi$ can be calculated as

$$\nabla(\nabla\phi) = \frac{1}{\Delta\forall}\sum_f \nabla\phi_f \Delta\vec{S}_f = \frac{1}{\Delta\forall}\left(\nabla\phi_b \Delta\vec{S}_b + \sum_{f\neq b} \nabla\phi_f \Delta\vec{S}_f\right) \tag{15}$$

where $\Delta\vec{S}_b$ is the surface vector of the boundary face and the sum on the right-hand side of the second equals sign is taken over the control surface except this boundary face. Substituting this equation into Eq. (14) yields the gradients at the boundary face centroid:

$$\nabla\phi_b = \frac{\nabla\phi_c + \frac{1}{\Delta\forall}\sum_{f\neq b} \nabla\phi_f \Delta\vec{S}_f \cdot \vec{\delta}_{cb}}{1 - \frac{1}{\Delta\forall}\Delta\vec{S}_b \cdot \vec{\delta}_{cb}} \tag{16}$$

3.2. Solution Methods

After discretization over space, Eqs. (12*a*) and (12*b*) becomes ordinary differential equations (ODEs) for the structure velocities. The velocities are related to the displacements by

$$\frac{d(d_x)}{dt} = u \tag{17a}$$

$$\frac{d(d_y)}{dt} = v \tag{17b}$$

Equations (12) and (17) form a system of first-order ordinary differential equations:

$$\frac{d\vec{U}}{dt} = \vec{F}(\vec{U}) \tag{18}$$

where $\vec{U} = [d_x, d_y, u, v]^T$.

There are many methods available for the solution of a system of ODEs. However, direct application of these methods becomes impractical because instability may arise due to the coupling between grid nodes. In addition, the time step must be kept small for these methods. To circumvent these problems, a fully implicit procedure is preferred. The dual-time-stepping technique is adopted here to fulfill this task, which has been successively incorporated in fluid flow calculations [23–25]. The real time derivative is first discretized. Then a pseudo-time derivative term is introduced to give

$$\frac{d\vec{U}^n}{d\tau} = \vec{F}(\vec{U}^n) - \frac{\vec{U}^n - \vec{U}^o}{\Delta t} = \vec{G}(\vec{U}^n) \tag{19}$$

where the superscripts n and o denote the new and old time values. Although there are a variety of choices of higher-order schemes, the backward Euler scheme is employed in the above just for simplicity. In each physical time step, the solution procedure marches until the pseudo-time derivative is driven to zero. The most

popular way to solve these ODEs is to use the Runge-Kutta method. A more efficient method employed in this study is the predictor-corrector scheme of Hamming [26].

$$\text{Predictor}: \quad \vec{U}^{m+1(0)} = \vec{U}^{m-3} + \frac{4}{3}\Delta\tau(2\vec{G}^{m} - \vec{G}^{m-1} + 2\vec{G}^{m-2}) \tag{20a}$$

$$\text{Corrector}: \quad \vec{U}^{m+1(l+1)} = \frac{1}{8}(9\vec{U}^{m} - \vec{U}^{m-2}) + \frac{3}{8}\Delta\tau(\vec{G}^{m+1(l)} + 2\vec{G}^{m} - \vec{G}^{m-1}) \tag{20b}$$

where the superscripts $m+1$, m, $m-1$, and $m-2$ represent the steps in the pseudo-time and the superscripts (l) and $(l+1)$ indicate the iteration indices. In the corrector step, iteration can be conducted to yield converged solution at the pseudo-time step $m+1$. However, this iteration is not necessary, because we are interested in obtaining converged solution in the physical time step. Only one correction is taken and the solution process advances to the next pseudo-time step. To start this fourth-order predictor-corrector scheme, the Runge-Kutta scheme is used in the first three steps. The prediction-correction procedure begins from the fourth time step and continues until convergence is reached.

4. NUMERICAL METHODS FOR FLUID FLOW

Different from the structure calculation, all variables are placed on the centroids of mesh cells in flow calculations (see Figure 1*b*). The time derivative of the Navier-Stokes equation (8) is discretized using the backward Euler scheme. The convective flux through the surface of a control volume can be approximated by

$$F^{c} = \sum_{f} \dot{m}_f^{r} \phi_f \tag{21}$$

where ϕ represents each of the velocity components and $\dot{m}_f^{r}$ is the mass flux relative to the moving grid.

$$\dot{m}_f^{r} = \dot{m}_f - \frac{\rho\,\Delta\forall_f}{\Delta t} \tag{22}$$

where $\Delta\forall_f$ is the volume swept by the moving grid and $\dot{m}_f$ is the absolute mass flux across the face. The face value ϕ_f is estimated by a strategy in which high-order schemes can be blended with the upwind difference scheme.

$$\phi_f = \phi_f^{UD} + \gamma\left(\phi_f^{HD} - \phi_f^{UD}\right) \tag{23}$$

where γ is the blending factor. There are a lot of options of high-resolution schemes to choose [27]. Here, the central difference is incorporated. In calculations, the upwind part of the convective flux is treated implicitly while the rest is treated explicitly.

The diffusive flux crossing the control surface is approximated by an overrelaxed approach [28], suitable for unstructured grids of arbitrary topology.

$$F^d = \sum_f \mu_f (\nabla \phi_f) \cdot \Delta \vec{S}_f = \sum_f \mu_f (\nabla \phi_f) \cdot \left[\vec{d} + \left(\Delta \vec{S}_f - \vec{d} \right) \right] \tag{24}$$

where

$$\vec{d} = \frac{\left| \Delta \vec{S}_f \right|^2}{\vec{\delta}_{PC} \cdot \Delta \vec{S}_f} \vec{\delta}_{PC}$$

Then, it can be approximated by

$$F^d = \sum_f \left[\frac{\mu_f |\Delta \vec{S}_f|^2}{\vec{\delta}_{PC} \cdot \Delta \vec{S}_f} (\phi_C - \phi_P) + \mu_f \overline{\nabla \phi}_f \cdot \left(\Delta \vec{S}_f - \vec{d} \right) \right] \tag{25}$$

Here the subscripts P and C denote the centroids of the principal and neighboring cells on the two sides of the considered face and $\vec{\delta}_{PC}$ is the distance vector directed from P to C (see Figure 1*b*). The face gradient $\overline{\nabla \phi}_f$ is obtained by linear interpolation from the gradient values at the two centroids. The first term in the above expression is the normal part of the diffusive flux. The second term designates the cross-derivative part which arises when $\vec{\delta}_{PC}$ is not orthogonal to the face. It is treated in an explicit manner.

For calculation of incompressible flow it is essential to deal with the coupling between momentum and continuity equations. A common approach to tackle this issue is to iterate among the momentum equation and a pressure-correction equation derived from the continuity constraint [28]. However, this iterative practice is very time-consuming. A noniterative prediction-correction procedure [29] is adopted in this study. This algorithm is briefly described in the following.

Predictor step. With use of the prevailing pressure P^*, a new velocity field $\vec{V}^*$ can be obtained by solving the momentum equation after being discretized by the approach given above.

$$A_P \vec{V}_P^* = \sum_C A_C \vec{V}_C^* + \left(S - \nabla P_P^* \, \Delta \forall \right) \tag{26}$$

The pressure gradients can be calculated using Eq. (13). The source S contains the explicit parts of the convective and diffusive fluxes. After dividing by A_P, the equation can be re-expressed as

$$\vec{V}_P^* = \vec{H}_P(\vec{V}^*) - D_P \nabla P_P^* \tag{27}$$

where

$$\vec{H}_P(\vec{V}^*) = \frac{\sum_C A_C \vec{V}_C^* + S}{A_P} \quad \text{and} \quad D_P = \left(\frac{\Delta\forall}{A_P}\right)_P$$

The velocity at the face required for calculation of the mass flux across the face is estimated by the momentum interpolation method [28]:

$$\vec{V}_f^* = \overline{\vec{V}_f^*} + \overline{D}_f \overline{\nabla P_f^*} - \overline{D}_f \nabla P_f^* \tag{28}$$

The mass flux across the face is then approximated as

$$\dot{m}_f^* = \rho_f \overline{\vec{V}_f^*} \cdot \Delta\vec{S}_f + A_f^P \left[\overline{\nabla P_f^*} \cdot \vec{\delta}_{PC} + \left(P_P^* - P_C^*\right)\right] \tag{29}$$

where

$$A_f^P = \rho_f \bar{D}_f \left(\frac{|\Delta\vec{S}_f|^2}{\vec{\delta}_{PC} \cdot \Delta\vec{S}_f}\right)$$

and the overbars designate interpolation from the values at nodes P and C.

The velocity obtained in this step does not satisfy the continuity constraint. In addition, the pressure field needs to be upgraded. They are adjusted in the following corrector steps.

First corrector step. The corrected velocity is obtained using an upgraded pressure in the following equation:

$$\vec{V}_P^{**} = \vec{H}_P(\vec{V}^*) - D_P \nabla P_P^{**} \tag{30}$$

Here the part $\vec{H}_P$ remains the same as in the predictor step. Subtracting the predictor equation (27) gives the velocity correction in terms of pressure correction:

$$\vec{V}'_P = -D_P \nabla P'_P \tag{31}$$

where $\vec{V}' = \vec{V}^{**} - \vec{V}^*$ and $P' = P^{**} - P^*$. Similarly, the velocity correction at the face can be given by

$$\vec{V}'_f = -D_f \nabla P'_f \tag{32}$$

The mass flux through the face is then corrected as

$$\dot{m}_f^{**} = \dot{m}_f^* + \rho_f \vec{V}'_f \cdot \Delta\vec{S}_f \approx \dot{m}_f^* - A_f^P (P'_C - P'_P) - \rho_f \bar{D}_f \overline{\nabla P_f} \cdot (\Delta\vec{S}_f - \vec{d}) \tag{33}$$

Here the overrelaxed approach, used in the calculation of diffusive flux given above, is also employed.

Enforcing the corrected mass fluxes through all the faces $\dot{m}_f^{**}$ surrounding the control volume to satisfy the mass conservation equation (10) leads to a pressure-correction equation,

$$A_P P'_P = \sum_C A_C P'_C + S^1_{P1} + S^1_{P2} \tag{34}$$

where

$$S^1_{P1} = -\sum_f \dot{m}_f^* \tag{35a}$$

$$S^1_{P2} = \sum_f \rho_f \bar{D}_f \overline{\nabla P'_f} \left(\Delta \vec{S}_f - \vec{d} \right) \tag{35b}$$

The appearance of the first source term is due to the nonconservation of the predictor velocity field and the second source is due to the nonorthogonality of the grid. The process to solve this equation is separated into two steps. A pressure correction $P^{(1)}$ is first sought by setting $S^1_{P2} = 0$. Then, a second correction $P^{(2)}$ is obtained by letting $S^1_{P1} = 0$ and using $P^{(1)}$ to estimate S^1_{P2}. The second step can be repeated until it converges. However, one such step is usually taken, because this correction value is small.

Second corrector step. In the last correction step, the contribution of the neighboring node part $\bar{H}_P$ to the momentum equation is taken from the predictor step in which the velocity field is not solenoidal. The velocity and pressure fields are further adjusted in this step such that satisfaction of the conservation principle is enhanced.

$$\vec{V}_P^{***} = \bar{H}_P(\vec{V}^{**}) - D_P \nabla P_P^{***} \tag{36}$$

Subtracting the corresponding equation in the first corrector yields

$$\vec{V}''_P = \bar{H}_P(\vec{V}') - D_P \nabla P''_P \tag{37}$$

where $\vec{V}'' = \vec{V}^{***} - \vec{V}^{**}$ and $P'' = P^{***} - P^{**}$. The face velocity correction is calculated similarly by

$$\vec{V}''_f = \bar{\bar{H}}_f(\vec{V}') - \bar{D}_f \nabla P''_f \tag{38}$$

where $\bar{\bar{H}}_f(\vec{V}')$ is estimated using interpolation from the corresponding terms of the equations for the nodes P and C. The mass flux at the face is then approximated by

$$\dot{m}_f^{***} = \dot{m}_f^{**} - A_f^P (P''_C - P''_P) - \rho_f \bar{D}_f \overline{\nabla P''_f} \cdot \left(\Delta \vec{S}_f - \vec{d} \right) + \rho_f \overline{\bar{H}_f(\vec{V}')} \cdot \Delta \vec{S}_f \tag{39}$$

The conservation requirement for all the fluxes $\dot{m}_f^{***}$ around the control volume results in an equation for the second pressure correction,

$$A_P P''_P = \sum_f A_C P''_C + S^2_{P1} + S^2_{P2} \tag{40}$$

where

$$S^2_{P1} = -\sum_f \rho_f \overline{\vec{H}_f(\vec{V}')} \cdot \Delta\vec{S}_f \tag{41a}$$

$$S^2_{P2} = \sum_f \rho_f \bar{D}_f \overline{\nabla P''_f} \cdot \left(\Delta\vec{S}_f - \vec{d}\right) \tag{41b}$$

This equation is also solved using the successive correction approach given in the first corrector.

More corrections in the form of the second corrector step can be imposed. However, only two correctors are employed because the accuracy of the solution is within the temporal truncation error after two correction steps.

5. INTERACTION BETWEEN FLUID AND STRUCTURE

In fluid–structure interaction problems, the fluid flow provides loading to the solid structure. The strain induced in the structure causes it to deform. The meshes for both the fluid and the structure must be adjusted in accordance with the deformation of the structure. An illustration of the grid adaptation in the flow domain is shown in Figure 2 for a flexible structure. The domain is partitioned into four regions. The mesh in region 1 is fixed and those in the other regions move with the deformed structure. The meshes in the flexible regions are generated using the linear transfinite interpolation.

The coupled fluid–structure system is tackled in a sequence manner. The traction forces exerted on the surface of the structure are obtained from the pressure

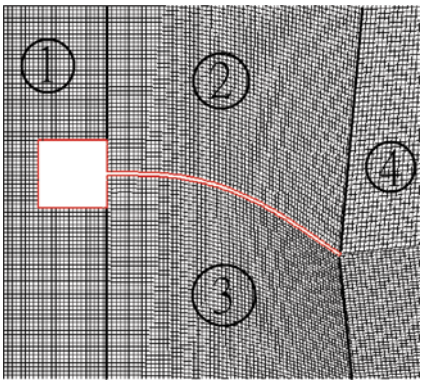

Figure 2. Illustration of the grid for the flow field (color figure available online).

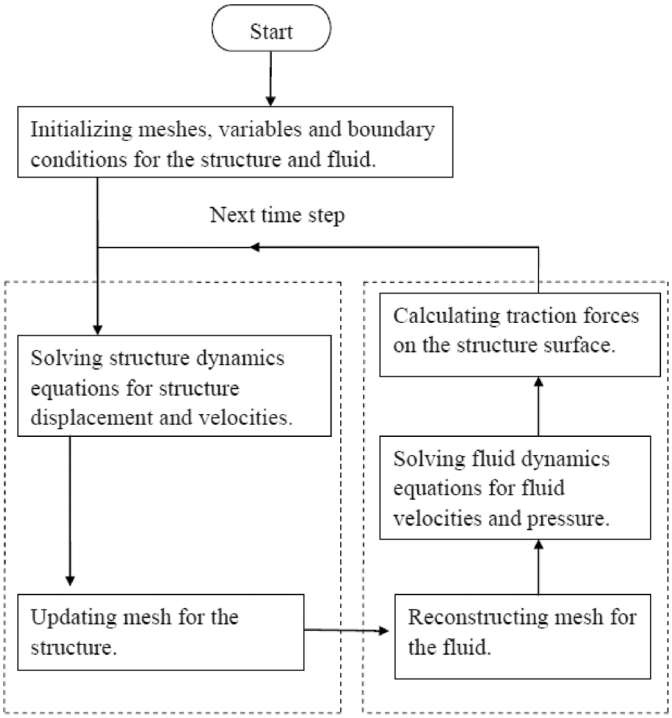

Figure 3. Solution procedure for the coupled structure–fluid calculation.

and shear forces of the flow field. The displacements of the structure are then calculated by solving the corresponding dynamics equations, which provide new boundaries for the fluid domain. The mesh for the flow is reconstructed according to the new position of the structure. The volume swept by the moving grid, required in Eq. (22), is estimated using the new and old meshes. Using the structure velocities at the fluid–structure interface as boundary conditions, the fluid dynamics equations can be solved. The traction forces are then recalculated. This completes computations in one time step and the solution process is advanced to the next time step. This solution procedure is illustrated in Figure 3.

6. RESULTS AND DISCUSSION

The finite-volume method for the structure dynamics is first tested on a cantilever beam under the action of a variety of types of load. It is followed by considering the interaction between fluids and structures. One case is an elastic plate placed vertically in a channel. The other is a flexible plate attached to the downstream face of a cylinder.

6.1. Deformation of a Cantilever Beam

A beam structure fixed at a single end is considered in Figure 4. It is subjected to either a single load at the free end or various types of distributed load. The length

(L) is 20 m and the breadth (b) is 2 m. The material properties are 2,600 kg/m^3 for density, 10 MPa for Young's modulus, and 0 for Poisson's ratio. The assumption of zero Poisson's ratio is simply for comparison with the analytical solution, which is obtained from pure bending theory. In addition, the relationship between the strain and the displacement gradient is assumed to be linear, since the displacement is small when compared with the dimension of the structure.

First considered is the cantilever with a single load at the free end, which serves as a typical test case in structure mechanics. The displacement at the free end is found theoretically [30] as

$$d_y = -\frac{FL^3}{3EI} \tag{42}$$

The displacement is -0.08 m under the force $F = 200$ N. Five levels of grid are used in calculations: 20×2, 40×4, 80×8, 160×16, and 200×20. The resulting displacements at the middle point of the free end face (point A in Figure 4) are -5.359E-02, -7.809E-02, -8.081E-02, -8.063E-02, and -8.057E-02. It is evident that the computational error decreases with the grid spacing. With a coarse grid, 40×4, the difference from the theoretical value is 2.39%. By increasing the grid density to a medium level of 80×8, the error is decreased to 1%.

Damping is a phenomenon by which mechanical energy is dissipated. The cause of damping can be associated to microstructure defects such as grain boundaries and impurities, rubbing friction between components, or intermittent contact at joints. This effect is modeled by a linear viscous damper given in Eq. (2). The vibration behavior of the structure depends on the damping ratio defined by

$$\zeta = \frac{c}{c_c} = \frac{c}{2m\omega} \tag{43}$$

where c_c is known as the critical damping coefficient, m is the beam mass per unit length, and ω is the natural circular frequency. For the cantilever, the

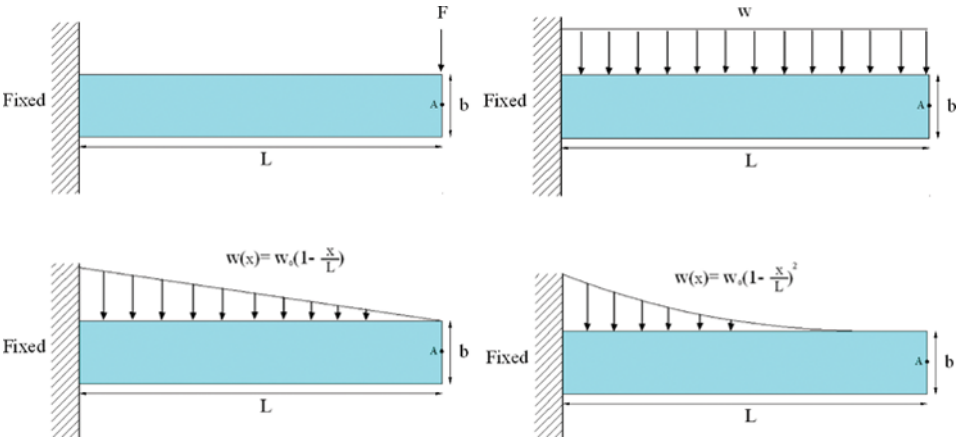

Figure 4. Cantilever beam under different types of loads (color figure available online).

circular frequency of the first mode can be determined from Bernoulli-Euler beam theory [31].

$$\omega = 3.516\sqrt{\frac{EI}{mL^4}} \tag{44}$$

Figure 5*a* presents the tip displacement variation for a number of damping ratios. It can be seen that the displacement varies in a monotonic manner to the steady state at critical damping ($\zeta = 1$). The system becomes underdamped when the damping ratio is less than 1. Obvious oscillations can be identified for $\zeta = 0.25$. Further reduction of this ratio brings about more significant oscillations.

It is interesting to examine the behavior of free oscillation without damping obtained by the present method. Steady-state solution is first obtained. Calculation is then carried on by removing the load and assigning a zero value to the damping coefficient. It is shown in Figure 5*b* that the oscillation exhibits a simple harmonic motion without decaying. The simulated oscillation frequency is 0.049 Hz and the period is 20.1 s, comparing favorably with the analytical ones of 0.05 Hz and 20 s obtained from Eq. (44).

In solving the system of ODEs without adopting the pseudo-time stepping, the time interval is usually restricted by the CFL condition, i.e., the Courant number must be less than 1. The merit of the dual-time stepping is to "cheat" the ODEs by treating the real time derivative as a source in the pseudo-time ODEs. As a result, it is the pseudo–time interval that is required to be limited, whereas the real time interval is not subject to the constraint of the CFL condition. Figure 6 shows the number of pseudo-time steps, or iterations, required for convergence in each real time step. The calculation is undertaken with an 80×8 grid using 0.001 for the pseudo-time interval and 0.01 for the real time interval. The Courant number, based on the wave propagation speed $c = \sqrt{E/\rho(1-\upsilon^2)}$ and the pseudo-time interval, is 0.24. It is seen that more than 100 pseudo-time steps are necessitated in the first

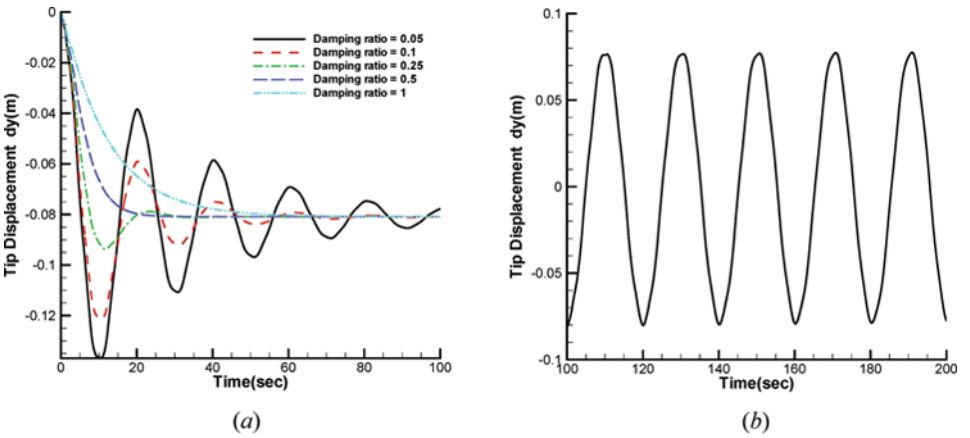

Figure 5. Movement of the cantilever tip: (*a*) under different damping ratios and (*b*) without damping (color figure available online).

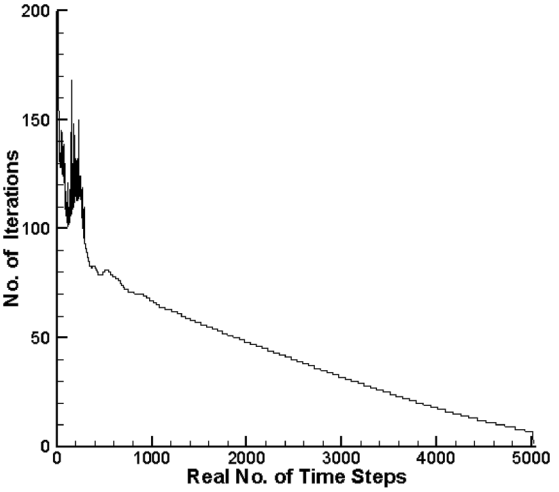

Figure 6. Number of pseudo-time steps (iterations) required for each real time step.

300 real time steps. This is followed by a gradual decrease of the number of iterations. Not more than 10 iterations are required in the end. A real time interval 0.1 was used to reduce the number of calculation steps to reach steady state. However, this paid off with a large increase in the number of pseudo-time steps.

In fluid–structure problems, the fluid load is distributed over the structure. Three different types of distributed load are under consideration: uniform, linear, and quadratic (see Figure 4). The corresponding theoretical solutions at the free end are [30]

$$d_y = -\frac{w_o L^4}{8EI} \tag{45a}$$

$$d_y = -\frac{w_o L^4}{30EI} \tag{45b}$$

$$d_y = -\frac{w_o L^4}{72EI} \tag{45c}$$

With a load constant $w_o = 100\,\mathrm{N/m^2}$, the calculated displacements are −3.03E-01, −8.08E-2, and −3,37E-02 for the three cases. Comparing with the theoretical values −3.E-01, −8.E-02, and −3.33E-02 implies that the errors are about 1%. The results seen in the above tests justify the finite-volume method for structure dynamics calculations.

6.2. Flow over a Vertical Plate

An elastic plate is situated vertically in a $20\,\mathrm{m} \times 2\,\mathrm{m}$ channel with one end clamped to the lower wall (see Figure 7). The plate is given a length of 1.6 m and a breadth of either 0.1 m or 0.2 m. Considering the material of polyester, the density is $1{,}200\,\mathrm{kg/m^2}$, the Young's modulus is 3,500 MPa and the Poisson's ratio is 0.32.

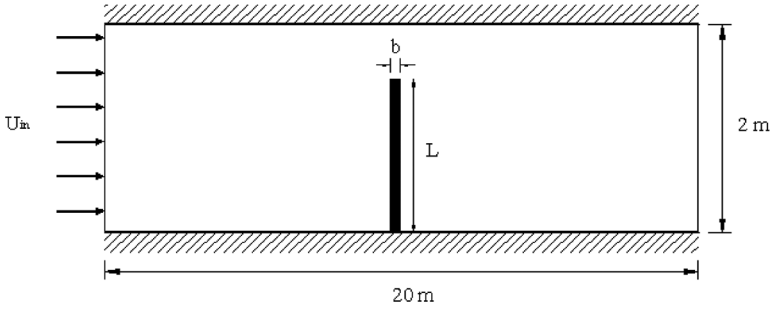

Figure 7. Sketch of the flow over a vertical plate in a channel.

The fluid has a density of 1 kg/m^3 and a viscosity of 0.2 kg/m-s. The fluid domain has a total number of about 16,200 grid cells and the solid domain has 512 cells with 8 cells in the breadth. The pseudo-time and real time intervals for the calculations are 1.E-04 s and 1.E-06 s, giving Courant numbers 0.1 and 10.

Three different constant velocities, corresponding to Reynolds numbers 50, 100, and 150, are specified at the inlet. The sudden start of fluid flow causes the plate to move backward and forward in the channel direction. As shown in Figure 8*a*, the amplitudes of oscillation are higher in the beginning stage for large Reynolds numbers. However, their decay rates are also more prominent. In the end, they reach the steady state more quickly. It can be detected that the higher the Reynolds number is, the more the structure is deformed. The resulting displacements at the free end are 2.41E-04, 8.65E-04, and 1.86E-03 when the Reynolds number is increased from 50 to 100, and to 150. As the breadth of the plate is reduced to 0.1 m, tip displacements are increased to 1.62E-03, 5.77E-03, and 1.29E-02. It needs to be noted that zero damping coefficient is assumed in the calculation. The resulting oscillation frequency for breadth 0.2 m is 21.83 Hz, close to the first natural frequency, 21.56 Hz.

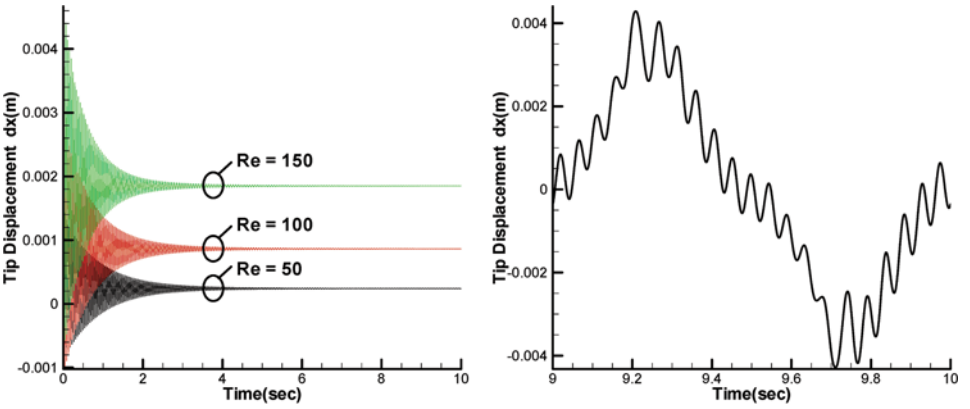

Figure 8. Movement of the plate tip for (*a*) constant inlet velocity and (*b*) sinusoidal inlet velocity (color figure available online).

In another test, a sinusoidal velocity $20\sin(2\pi t)$ is applied at the inlet. The Reynolds number is 200, based on the maximum velocity. The movement at the tip in a period of 1 s is given in Figure 8*b* after reaching the periodic steady state. It is apparent that the movement of the plate is forced to follow the sinusoidal motion of the flow. There exists a small oscillation superimposed on the forced wavy motion. This high-frequency movement is caused by the free vibration of the structure. Its frequency is equivalent to the first natural frequency.

6.3. Vortex-Induced Motion of an Elastic Plate

It is well known that the flow over a bluff body may cause vortex shedding and, thus, periodic variation of the flow structure. In the current test, a flexible plate is clamped to the lee side of a square cylinder, which is situated at the center of a channel of dimension 1.95E-01 m × 1.2E-01 m. (see Figure 9). The plate has a length 4.0E-02 m and a breadth 6.0E-04 m, and the side length of the square cylinder is 1.0E-02 m. The density of the plate is 2,000 kg/m^2. The Young's modulus is 0.2 MPa and the Poisson's ratio is 0.35. As for the fluid, the density is 1.18 kg/m^2 and the viscosity is 1.82E-05 kg/m-s. The computational grid has 62,376 cells for the fluid and 384 cells for the structure. Three different velocities (0.17, 0.315, and 0.448 m/s) are assigned at the inlet, giving Reynolds numbers 110, 204, and 290.

The oscillatory amplitude at the tip of the plate shown in Figure 10*a* implies that the strength of the vibration is very weak for $\mathrm{Re} = 110$. A spectral analysis on the data was conducted. It is seen from Figure 11*a* that the frequency of the vibration is 0.65 Hz, which is comparable to the first natural frequency, 0.61 Hz, obtained from Eq. (44). As seen from the flow field given by Figure 12, the wake behind the cylinder is of closed form with two nearly symmetric vortices on both sides of the plate. The wake encloses the plate with a longitudinal size slightly larger than the length of the plate. This phenomenon indicates that the flow is nearly in a steady state. It is generally recognized that the vortex shedding for a square cylinder occurs at a Reynolds number around 50. The delay of inception of the shedding is due mainly

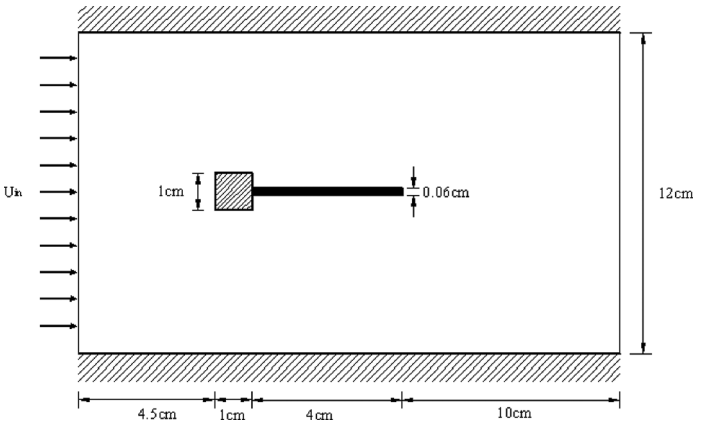

Figure 9. Sketch of the flow over a square cylinder with a plate attached.

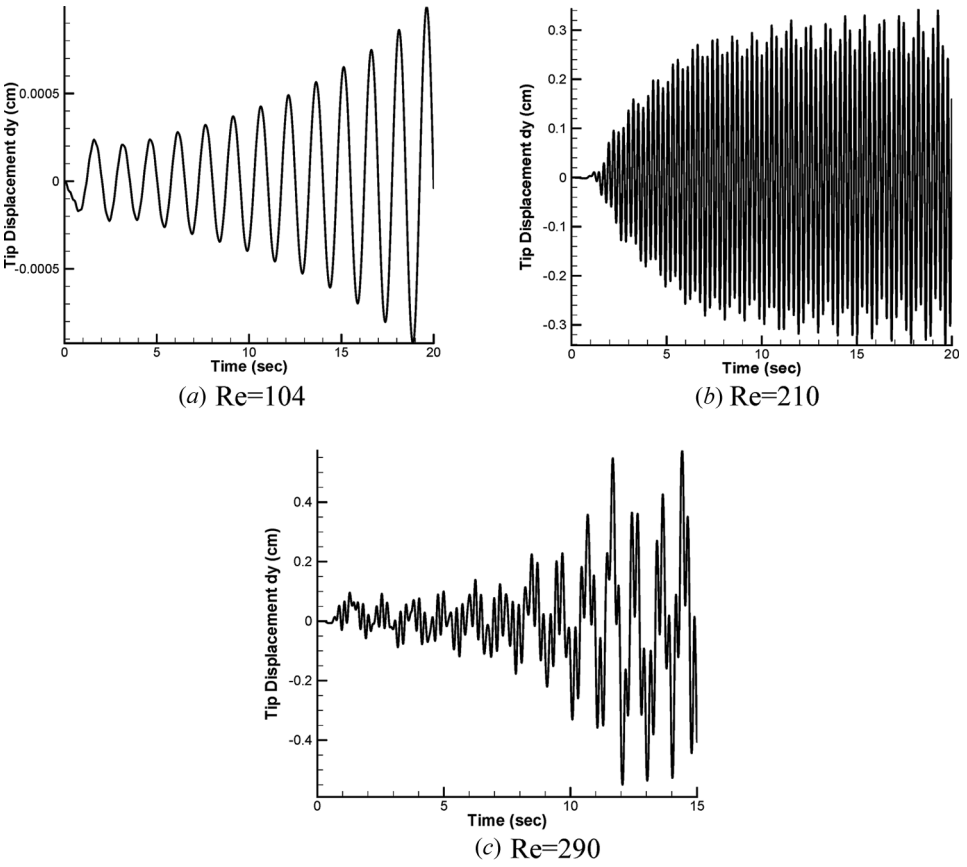

Figure 10. Movement of the plate tip for different Reynolds numbers.

to the appearance of the splitter plate, which prevents the interaction of the vortices behind the upper and lower sides of the cylinder until the end of the plate [32, 33]. Another factor affecting the vortex shedding is the appearance of the channel walls. Since the blockage ratio of the channel height to the cylinder height is large (12:1), this effect is insignificant.

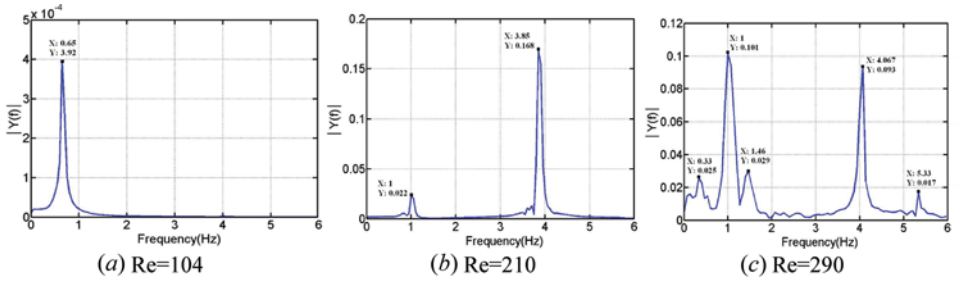

Figure 11. Spectral analysis for different Reynolds numbers (color figure available online).

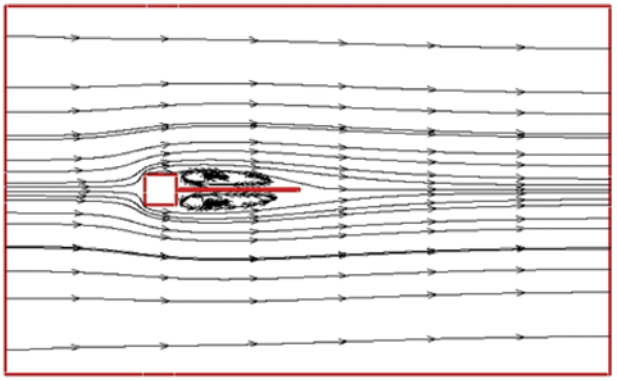

Figure 12. Flow streamlines for Re = 110 (color figure available online).

As the Reynolds number is increased to 204, the oscillation becomes more prominent with greater amplitude and higher frequency, being seen from Figure 10*b*. The spectral analysis shown in Figure 11*b* indicates that the vibration is dominated by a wave at frequency 3.85 Hz, along with a much weaker wave at frequency 1 Hz. This implies that the vibration approaches a nearly periodic state with a frequency 3.85 Hz, which is close to the natural frequency of 3.8 Hz of the second mode obtained from [31].

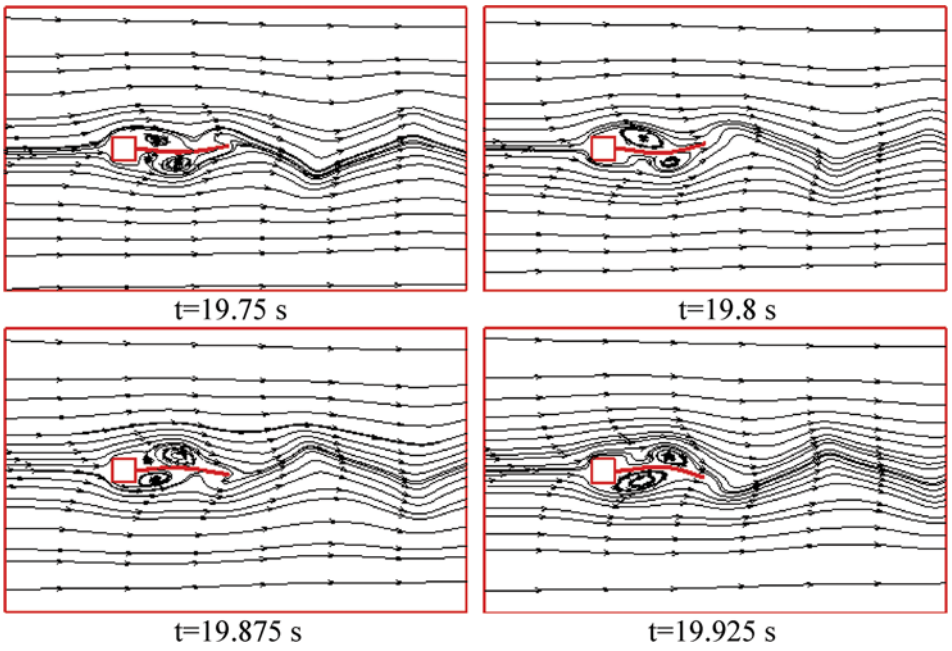

Figure 13. Flow streamlines for Re = 204 (color figure available online).

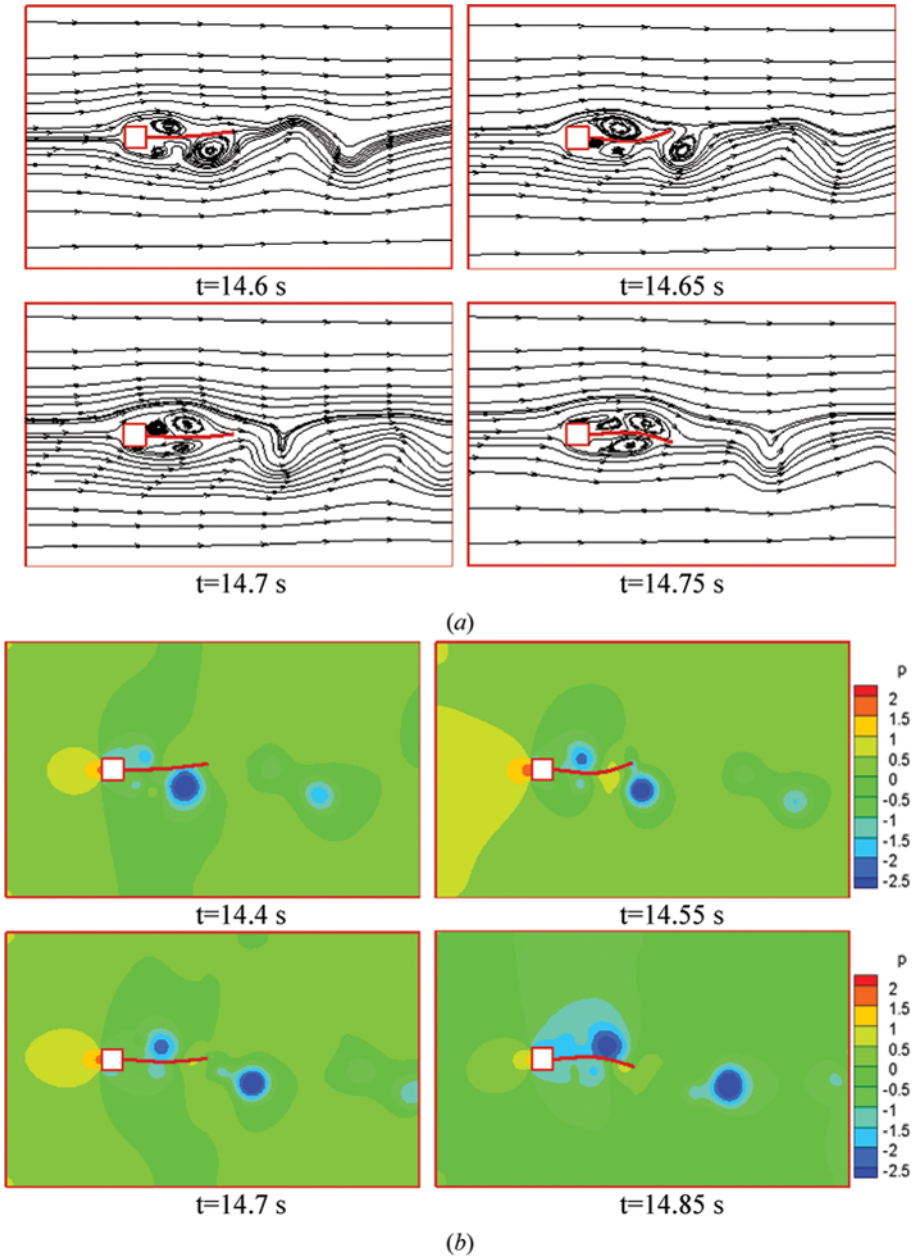

Figure 14. Flow field for Re = 290: (*a*) streamlines and (*b*) pressure distribution (color figure available online).

$$\omega = 22.035\sqrt{\frac{EI}{mL^4}} \tag{46}$$

As shown in Figure 13, the plate is deformed into a bowlike shape, reflecting the fact that the second mode dominates the vibration. The flow field behind the square

cylinder caused by the movement and deformation of the flexible plate features a number of vortices around the plate. In general, one vortex is seen on the inner side of the plate bow and two vortices are found on the outer side, with a small one immediately behind the square. When the plate changes its deformation pattern from concave to convex shape, the flow field is changed accordingly. It is worth while to note that no vortex shedding from the plate tip was found during the periodic change of flow pattern.

It is seen in Figure 10*c* that the vibration of the plate is enlarged with further increase of Reynolds number to 290. As shown from Figure 11*c*, the oscillation occurs mainly at two frequencies, 1 Hz and 4.067 Hz, compared to the first natural frequency of 0.61 Hz and the second natural frequency of 3.8 Hz. As seen from Figure 14*a*, the structure of the eddy flow is more complex than those for low Reynolds numbers. It can be identified that the vortex close to the tip on the lower side of the plate detaches from the plate at $t = 14.65$ s. The vortices feature low pressure in their areas, which can be viewed from the pressure contour plots given by Figure 14*b*. It is clearly illustrated that the shedding low-pressure area moves downward with the stream. The shedding of the eddy may result in appearance of a Karman vortex street if the Reynolds number is further increased.

7. CONCLUSIONS

To have a consistent discretization method for fluid and solid, an unstructured-grid finite-volume solution solver for structure dynamics calculations has been developed. It features the use of dual-time-stepping technique in which the iteration in a real time step is performed by marching the pseudo-time until convergence is reached. Although the pseudo-time step is limited by the CFL condition, there is no such a restriction on the real time step. Tests on a cantilever subject to different loads reveal its accuracy in terms of deflection and natural frequency. For the case involving a plate immersed vertically in a channel flow, it can be seen that the plate vibrates at its natural frequency under the action of the fluid flow. In the case of vortex-induced vibration, the wake behind the cylinder is of closed form and symmetrical to the plate at $\mathrm{Re} = 110$. The flow field is in a nearly steady state. Although unsteady, periodic flow and significant vibration of the plate are observed at $\mathrm{Re} = 204$, no vortex shedding occurs. The detachment of the vortex from the tip of the vibrational plate is observed at $\mathrm{Re} = 290$. The results show that the flexible plate attached to the cylinder functions to suppress the vortex shedding. Further and more extensive studies are necessary to investigate this effect.

REFERENCES

1. E. Onate, M. Cervera, and O. C. Zienkiewicz, A Finite Volume Format for Structural Mechanics, *Int. J. Numer. Meth. Eng.*, vol. 37, pp. 181–201, 1994.
2. S. R. Idelsohn and E. Onate, Finite Volumes and Finite Elements: Two 'Good Friends', *Int. J. Numer. Meth. Eng.*, vol. 37, pp. 3323–3341, 1994.
3. I. Demirdzic and S. Muzaferija, Finite Volume Method for Stress Analysis in Complex Domains, *Int. J. Numer. Meth. Eng.*, vol. 37, pp. 3751–3766, 1994.

4. M. A. Wheel, A Geometrically Versatile Finite Volume Formulation for Plane Strain Elastostatic Stress Analysis, *J. Strain Anal. Eng. Des.*, vol. 31, pp. 111–116, 1996.
5. M. A. Wheel, A Finite-Volume Approach to the Stress Analysis of Pressurized Axisymmetric Structures, *Int. J. Pressure Vessels Piping*, vol. 68, pp. 311–317, 1996.
6. M. A. Wheel, A Finite Volume Method for Analysing the Bending Deformation of Thick and Thin Plates, *Comput. Meth. Appl. Mech. Eng.*, vol. 147, pp. 199–208, 1997.
7. H. Jasak and H. G. Weller, Application of the Finite Volume Method and Unstructured Meshes to Linear Elasticity, *Int. J. Numer. Meth. Eng.*, vol. 48, pp. 267–287, 2000.
8. C. Bailey and M. Cross, A Finite Volume Procedure to Solve Elastic Solid Mechanics Problems in Three Dimensions on an Unstructured Mesh, *Int. J. Numer. Meth. Eng.*, vol. 38, pp. 1757–1776, 1995.
9. A. K. Slone, K. Pericleous, C. Bailey, and M. Cross, Dynamic Fluid-Structure Interaction Using Finite Volume Unstructured Mesh Procedures, *Comput. Struct.*, vol. 80, pp. 371–390, 2002.
10. A. K. Slone, C. Bailey, and M. Cross, Dynamic Solid Mechanics Using Finite Volume Methods, *Appl. Math. Model.*, vol. 27, pp. 69–87, 2003.
11. G. H. Xia, Y. Zhao, J. H. Yeo, and X. Lv, A 3D Implicit Unstructured-Grid Finite Volume Method for Structural Dynamics, *Computat. Mech.*, vol. 40, pp. 299–312, 2007.
12. X. Lv, Y. Zhao, X. Y. Huang, G. H. Xia, and X. H. Su, A Matrix-Free Implicit Unstructured Multigrid Finite Volume Method for Simulating Structural Dynamics and Fluid–Structure Interaction, *J. Computat. Phys.*, vol. 225, pp. 120–144, 2007.
13. G. Xia and C. L. Lin, An Unstructured Finite Volume Approach for Structural Dynamics in Response to Fluid Motions, *Comput. Struct.*, vol. 86, pp. 684–701, 2008.
14. I. Demirdzic, and S. Muzaferija, Numerical Method for Coupled Fluid Flow, Heat Transfer and Stress Analysis Using Unstructured Moving Meshes with Cells of Arbitrary Topology, *Comput. Meth. Appl. Mech. Eng.*, vol. 125, pp. 235–255, 1995.
15. C. J. Greenshields and H. G. Weller, A Unified Formulation for Continuum Mechanics Applied to Fluid-Structure Interaction in Flexible Tubes, *Int. J. Numer. Meth. Eng.*, vol. 64, pp. 1575–1593, 2005.
16. K. Stein, R. Benney, V. Kalro, T. E. Tezduyar, J. Leonard, and M. Accorsi, Parachute Fluid-Structure Interactions: 3-D Computation, *Comput. Meth. Appl. Mech. Eng.*, vol. 190, pp. 373–386, 2000.
17. H. Afrasiab, M. R. Movahhedy, and A. Assempour, Finite Element and Analytical Fluid-Structure Interaction Analysis of the Pneumatically Actuated Diaphragm Microvalves, *Acta Mech.*, vol. 222, pp. 175–192, 2011.
18. J. De Hart, G. W. M. Peters, P. J. G. Schreurs, and F. P. T. Baaijens, A Three-Dimensional Computational Analysis of Fluid–Structure Interaction in the Aortic Valve, *J. Biomech.*, vol. 36, pp. 103–112, 2003.
19. M. Gluck, M. Breuer, F. Durst, A. Halfmann, and E. Rank, Computation of Fluid-Structure Interaction on Lightweight Structures, *J. Wind Eng. Ind. Aerodyn.*, vol. 89, pp. 1351–1368, 2001.
20. D. C. Sternel, M. Schafer, M. Heck, and S. Yigit, Efficiency and Accuracy of Fluid-Structure Interaction Simulations Using an Implicit Partitioned Approach, *Comput. Mech.*, vol. 43, pp. 103–113, 2008.
21. R. L. Panton, *Incompressible Flow*, John Wiley, New York, 1996.
22. I. Demirdzic and M. Peric, Space Conservation Law in Finite Volume Calculations of Fluid Flow, *Int. J. Numer. Meth. Fluids*, vol. 8, pp. 1037–1050, 1988.
23. A. Jameson, Time Dependent Calculations Using Multigrid, with Applications to Unsteady Flows past Airfoils and Wings, AIAA Paper 91-1596, 1991.

24. A. Jameson, An Assessment of Dual-Time Stepping, Time Spectral and Artificial Compressibility Based Numerical Algorithms for Unsteady Flow with Applications to Flapping Wings, AIAA Paper 2009–4273, 2009.
25. J. M. Weiss and W. A. Smith, Preconditioning Applied to Variable and Constant Density Flows, *AIAA J.*, vol. 33, pp. 2050–2057, 1995.
26. R. W. Hornbeck, *Numerical Methods*, Quantum Publishers, New York, 1975.
27. Y.-Y. Tsui and T.-C. Wu, A Pressure-Based Unstructured-Grid Algorithm Using High-Resolution Schemes for All-Speed Flows, *Numer. Heat Transfer B*, vol. 53, pp. 75–96, 2008.
28. Y.-Y. Tsui and Y.-F. Pan, A Pressure-Correction Method for Incompressible Flows Using Unstructured Meshes, *Numer. Heat Transfer B*, vol. 49, pp. 43–65, 2006.
29. R. I. Issa, Solution of the Implicitly Discretised Fluid Flow Equations by Operator-Splitting. *J. Comput. Phys.*, vol. 62, pp. 40–65, 1986.
30. R. T. Fenner, *Mechanics of Solids*, Blackwell Scientific, Oxford, UK, 1989.
31. S. S. Rao, *Vibration of Continuous Systems*, John Wiley, Hoboken, NJ, 2007.
32. M. F. Unal and D. Rockwell, On Vortex Formation from a Cylinder, Part 2: Control by Splitter-Plate Interference, *J. Fluid Mech.*, vol. 190, pp. 513–529, 1988.
33. S. Ozono, Flow Control of Vortex Shedding by a Short Splitter Plate Asymmetrically Arranged Downstream of a Cylinder, *Phys. Fluids*, vol. 11, pp. 2928–2934, 1999.